Energy Storage Materials 14 (2018) 314–323

Contents lists available at ScienceDirect

Energy Storage Materials

journal homepage: www.elsevier.com/locate/ensm

Carbon hollow nanobubbles on porous carbon nanofibers: An ideal host for high-performance sodium-sulfur batteries and hydrogen storage

Guanglin Xia[a,b], Lijun Zhang[a], Xiaowei Chen[c], Yuqin Huang[a], Dalin Sun[a,d], Fang Fang[a,*], Zaiping Guo[b,*], Xuebin Yu[a,d,**]

[a] Department of Materials Science, Fudan University, Shanghai 200433, China
[b] Institute for Superconducting and Electronic Materials, University of Wollongong, North Wollongong, NSW 2522, Australia
[c] Department of Physics, School of Science, Jimei University, Xiamen 361021, China
[d] Shanghai Innovation Institute for Materials, Shanghai 200444, China

ARTICLE INFO

Keywords:
Porous carbon
Nanobubble
Hydrogen storage
Magnesium hydride
Nanofibers

ABSTRACT

One-dimensional (1D) carbon nanostructures have been intensively investigated because of their intriguing features and great potential for practical application in various fields. This paper reports the controllable fabrication of carbon hollow nanobubbles on porous carbon nanofibers (CHNBs@PCNFs) through a general electrospinning strategy, with metal azides serving as both a bubbling and a porogen reagent. The strong repulsive forces resulting from the intense release of N_2 from the decomposition of metal azides upon carbonization leads to the uniform formation of porous carbon nanofibers (PCNFs), which could be facile tuned by heating rates and the amount of the bubbling reagent, simultaneously constructed with carbon hollow nanobubbles (CHNBs) on the surface. Density functional theory calculations reveal the strong interactions between terminal Na atoms in sodium polysulfides and N and O atoms doped into CHNBs@PCNFs, which could effectively alleviate the shuttle effect of Na-S batteries via adsorbing and trapping polysulfides. With strong adsorption capability of sodium polysulfides and high electrical conductivity, these CHNBs@PCNFs are demonstrated to be an ideal sulfur host in room-temperature sodium-sulfur batteries, which delivers a high reversible capacity of 256 mA h g^{-1} (specific energy density 384 W h kg^{-1}) with a low decay rate of 0.044% per cycle at 2 C-rate. When CHNBs@PCNFs used as functional supports for MgH_2 nanoparticles, a significantly enhanced hydrogen storage performance was achieved. The present work represents a critically important step in advancing the electrospinning technique for generating 1D carbon nanostructures in a facile and universal manner.

1. Introduction

The ever increasing global demand for renewable energy generated by green but intermittent power sources, such as wind and solar, requires efficient energy storage systems. Owing to their high energy densities, electrochemical energy storage and hydrogen storage materials have received intense attentions [1–3]. As an energy carrier, hydrogen can in principle be produced from a diverse range of renewable sources [4]. More importantly, because it has the highest gravimetric energy storage density (142 MJ kg^{-1}) and it is the most environmentally benign fuels with the production of only water from combustion, hydrogen has been widely investigated as a universal energy carrier that could enable the transition to renewable energy sources [5]. The safe and efficient storage of hydrogen is one of the key challenges towards the development of sustainable hydrogen economy [6].

On the other hand, metal-sulfur batteries (*e.g.*, Li-S and Na-S batteries) have also been recognized as a promising technology for stationary energy storage due to the high theoretical capacity (1672 mA h g^{-1}) of sulfur cathode material with high natural abundance and low cost [7–9]. The limited lithium resources, uneven distribution and hence relatively high price, however, limit the large-scale applications of Li-S batteries [10]. In this regard, sodium has been considered as a low-cost alternative to lithium as anode, featuring comparable mechanism of chemical insertion and reactivity, due to both the low cost and the rich abundance of Na sources [10]. Among them, the high-temperature molten-electrode sodium-sulfur (Na-S) battery has been regarded as one of the most successful energy storage technologies owing to its application in stationary energy storage systems for several decades [9,11]. Unfortunately, a high operating temperature above 300 °C is required for melting the ceramic electro-

* Corresponding author.
** Corresponding author at: Department of Materials Science, Fudan University, Shanghai 200433, China.
E-mail addresses: f_fang@fudan.edu.cn (F. Fang), zguo@uow.edu.au (Z. Guo), yuxuebin@fudan.edu.cn (X. Yu).

https://doi.org/10.1016/j.ensm.2018.05.008
Received 8 January 2018; Received in revised form 11 April 2018; Accepted 8 May 2018
Available online 09 May 2018

lyte, $NaAl_{11}O_{17}$, in traditional Na-S batteries, which leads to high cost and serious safety problems due to melting of the Na and S electrodes and limits their widespread applications [12]. In order to avoid these disadvantages, rechargeable room-temperature Na-S batteries are proposed with a liquid polymer as the electrolyte [13,14]. The operation of a Na-S battery at ambient temperature, however, suffers from low reversible capacity and extremely fast capacity fading during cycling due to the intrinsic electronically insulating properties of sulfur and the fracturing of the electrodes caused by the large volumetric changes occurring between sulfur and sodium sulfide [15]. Another obstacle obstructing the practical development of Na-S batteries relates to sodium polysulfides (NaPSs), the highly soluble intermediate products, which lead to rapid sulfur loss, the unfavorable shuttle effect, and also the subsequent accumulation of electrically inert reduction products on the electrodes [16–19].

In order to address these problems, porous carbon materials, including carbon hollow nanospheres, carbon nanotubes, and carbon nanofibers, have been proposed and investigated as Supporting materials for sulfur cathodes to improve the electrochemical performance of Na-S batteries [15,20–24]. A carbon matrix could significantly improve the electrical conductivity of sulfur cathodes, leading to the enhanced utilization of the active sulfur materials [7,8,25]. In addition, the flexible nature and the high pore volume of carbon is beneficial for accommodating the large volume changes of sulfur associated with sodium insertion and extraction [20]. Recently, increasing attention has been paid to the synthesis of one-dimensional (1D) carbon nanofibers (CNFs) with designed porous architecture for supporting electrochemically active materials, which is mainly attributable to its robust geometry to maintain their functionalities during chemical reactions and provide efficient paths for electron and mass transport [26–28]. Significantly improved specific capacities, however, are usually only obtained when a high percentage of carbon matrix is introduced because of the limited pore volume of current CNFs [29,30]. This leads to low sulfur loading in the cathode materials and hence low energy density, which makes them less attractive for practical applications. Additionally, due to the weak interaction between nonpolar CNFs and polar NaPSs, rapid capacity decay is still present during discharge and charge cycling, which is mainly due to the dissolution of the reaction intermediate NaPSs [23], so that the cycling stability of Na-S batteries remains a great challenge for practical applications. Therefore, it is necessary to develop new porous CNFs (PCNFs) that possess both high volumes to effectively accommodate the volume changes of sulfur in high-mass-loading Na-S batteries and effective chemical interaction with the NaPSs to alleviate the shuttle effect, which is crucial to the design of advanced Na-S batteries with high loading and utilization of sulfur, long cycling life, and good rate capability.

Bearing these considerations in mind, here, we have designed and successfully synthesized PCNFs with a hierarchical architecture, *i.e.*, controllable carbon hollow nanobubbles constructed on porous carbon nanofibers, through bubbling-assisted electrospinning followed by a simple stepwise calcination process. The as-electrospun nanofibers (NFs) were first obtained by electrospinning a homogeneous solution of poly(vinyl alcohol) (PVA) containing the bubbling and porogen reagent LiN_3 (Fig. 1). By simply tuning the amount of LiN_3 and the heating rate during carbonization, PCNFs, containing micropores, mesopores, and macropores, were controllably fabricated, with the simultaneous formation of carbon hollow nanobubbles (CHNBs) with a diameter of 10–60 nm on their surfaces, which provide large void space for sulfur accommodation. Moreover, the integrated 1D PCNFs, which constitute continuous electron conductive pathways, could effectively facilitate rapid electron and ion transport within insulating S nanoparticles accommodated by isolated CHNBs. Furthermore, density functional theory (DFT) calculations verify the strong chemical adsorption capability of CHNBs@PCNFs for NaPSs, induced by the strong interactions between terminal Na atoms in sodium polysulfides and N and O atoms doped in during the carbonization process, which effectively alleviate the shuttle effect of NaPSs. Thus, when employing CHNBs@PCNFs as the sulfur host for Na-S batteries, the S(CHNBs@PCNFs) cathodes exhibit a significantly improved utilization rate of sulfur, and good cycling stability and rate capability. Additionally, the robust porous structure and the catalytic effects of CHNBs@PCNFs are successfully exploited as a functional structural framework to support MgH_2 nanoparticles, which exhibit complete hydrogenation at a temperature as low as 250 °C within only 15 min.

2. Results and discussion

To construct CHNBs on PCNFs, PVA nanofibers containing the bubbling agent (*i.e.*, LiN_3) were first fabricated via a scalable and simple electrospinning technique. Scanning electron microscope (SEM) images of the as-electrospun PVA-LiN_3 NFs at different magnifications in Fig. 2a reveal that the as-obtained PVA-LiN_3 NFs are long and continuous, with a smooth surface and a relatively uniform diameter of about 300 nm, which are analogous to the PVA NFs without the addition of LiN_3 (Fig. S1 in the Supporting Information). After the stepwise carbonization, the as-formed CNFs from PVA NFs without LiN_3 have smooth surfaces with an average diameter of ~ 180 nm (Fig. S2a). By comparison, although the calcination of PVA NFs with the addition of LiN_3 through the same procedure leads to the fabrication of CNFs with the same basic fibrous structure, a plethora of nanobubbles with various diameters ranging from 10 to 60 nm are uniformly and densely distributed on the surfaces of the as-prepared CNFs, which have a diameter of ~ 200 nm (Fig. 2b and c). Transmission electron microscope (TEM) images (Fig. 2d and e) further confirm that these carbon nanobubbles are hollow and that the shells are very thin, with a thickness of only ~2 nm. Furthermore, the presence of pores with diameters of around 10–30 nm could be observed inside the body of the CNFs (Fig. 2d), which could be attributed to the vigorous decomposition of LiN_3, approaching the center of the PVA NFs, while no porous structure was observed for CNFs obtained from the decomposition of the as-electrospun PVA nanofibers without the presence of LiN_3 (Fig. S2b). The presence of long and continuous PCNFs during TEM observations after the vigorous scratching and ultrasonic treatment used for preparing the samples indicates its high structural robustness. Selected area electron diffraction (SAED) patterns (inset of Fig. 2d) show dispersing diffraction rings, demonstrating the amorphous nature of CHNBs@PCNFs after washing and drying, which coincides well with XRD results (Fig. S3). The porous texture of CHNBs@PCNFs was further investigated by nitrogen adsorption/desorption isotherms at 77 K (Fig. S4a), which reveal a specific surface area of 420 $m^2\ g^{-1}$ and a large pore volume of 1.64 $cm^3\ g^{-1}$, respectively. The distribution of pore sizes (Fig. S4b) determined from the adsorption branches is wide, with many peaks in the 2–100 nm range. Three regions can be identified: a) micropores (0–2 nm), b) mesopores (8–25 nm), and c) macropores (50–68 nm), which confirms the hierarchical porous characteristics of the CHNBs@PCNF texture and agrees well with the SEM/TEM observations. In strong contrast, without the presence of LiN_3, the specific surface area of the as-synthesized CNFs is only around 208 $m^2\ g^{-1}$ with an average pore size of ~ 2 nm (Fig. S5).

In order to gain insight into the development of this unique structure, the thermal decomposition of as-electrospun PVA NFs with and without the bubbling agent was measured by thermogravimetric analysis (TGA) in N_2 atmosphere (Fig. S6). No violent weight loss was observed for them below 170 °C, indicating that both samples were thermally stable under these conditions. Subsequently, a strong weight loss was detected in the range of 170–240 °C for the PVA-LiN_3 NFs, which could be attributed to the strong N_2 evolution resulting from the explosive decomposition of the bubbling agent[31], while no decomposition behavior was observed for the PVA NFs without LiN_3. Further weight loss between 240 °C and 650 °C was induced by the carboniza-

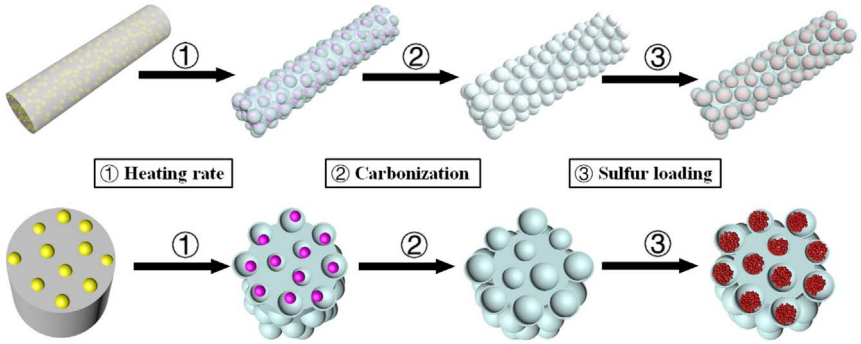

Fig. 1. Schematic illustration of the preparation of CHNBs@PCNFs and their application as sulfur hosts for room temperature Na-S batteries. Yellow, pink, and red balls represent LiN_3, Li_3N, and S particles, respectively.

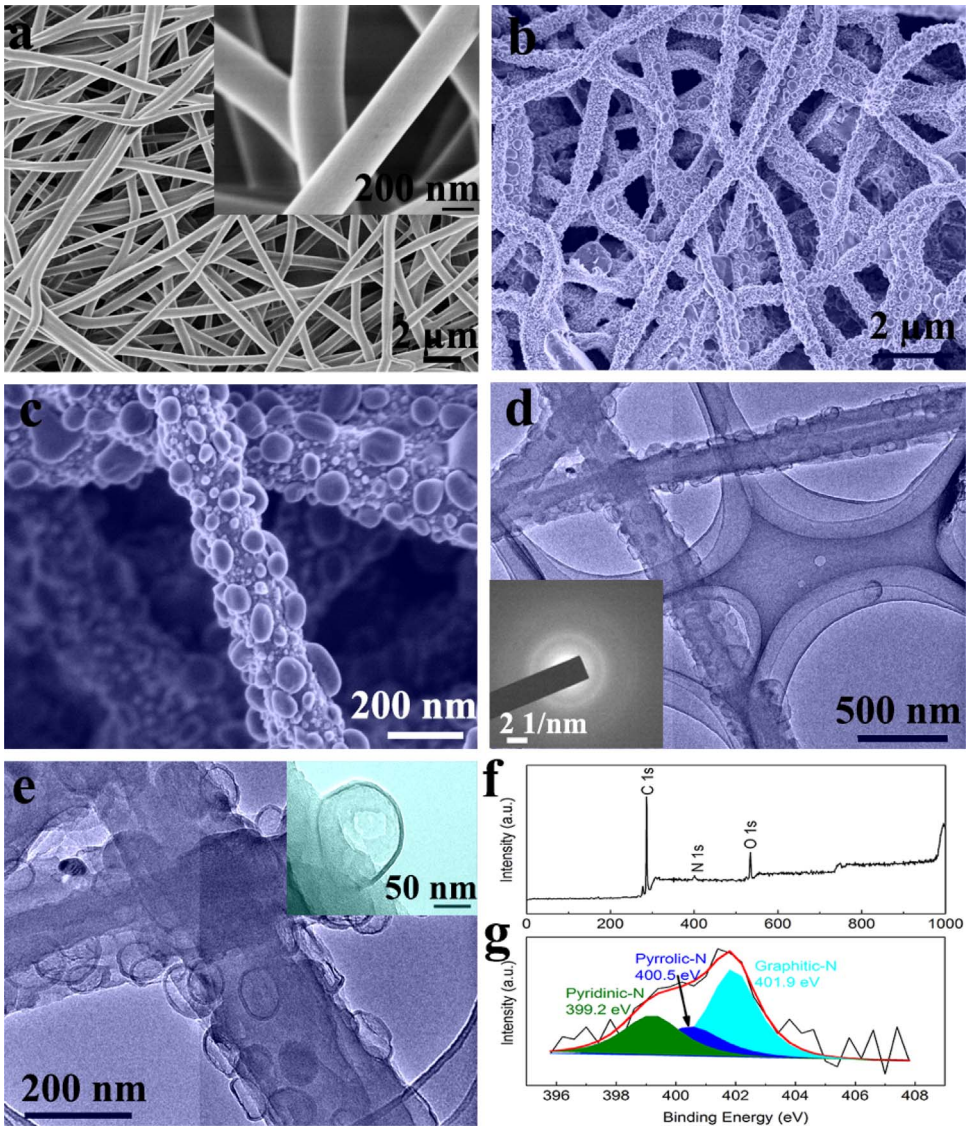

Fig. 2. (a) SEM image of the as-electrospun PVA-LiN_3 nanofibers. The inset of (a) shows a magnified image of as-electrospun PVA nanofibers. (b, c) SEM images of PCNFs after calcination of as-electrospun PVA-LiN_3 nanofibers. (d, e) TEM images of the as-synthesized CHNBs@PCNFs at different magnifications. The inset of (d) and (e) shows the SAED patterns of CHNBs@PCNFs and a magnified image of CHNBs@PCNFs, respectively. XPS survey spectrum (f) and high-resolution N 1 s spectrum (g) of CHNBs@PCNFs.

tion of PVA NFs to form carbon nanofibers. Therefore, in order to obtain structurally integrated three-dimensional (3D) PCNFs, a stepwise annealing strategy was applied to calcine the as-electrospun PVA-LiN_3 NFs by tuning the decomposition rate of LiN_3 according to the TGA results. First, the as-electrospun PVA-LiN_3 films were stabilized and dewatered under N_2 atmosphere at 150 °C for 1 h, and the 1D fibrous morphology was well maintained (Fig. S7). Subsequently, the dried PVA-LiN_3 NFs were slowly heated to 240 °C with a heating rate of 0.5 °C min^{-1} and kept at 240 °C for 2 h in N_2 atmosphere to ensure the complete decomposition of LiN_3. The color of the as-electrospun films

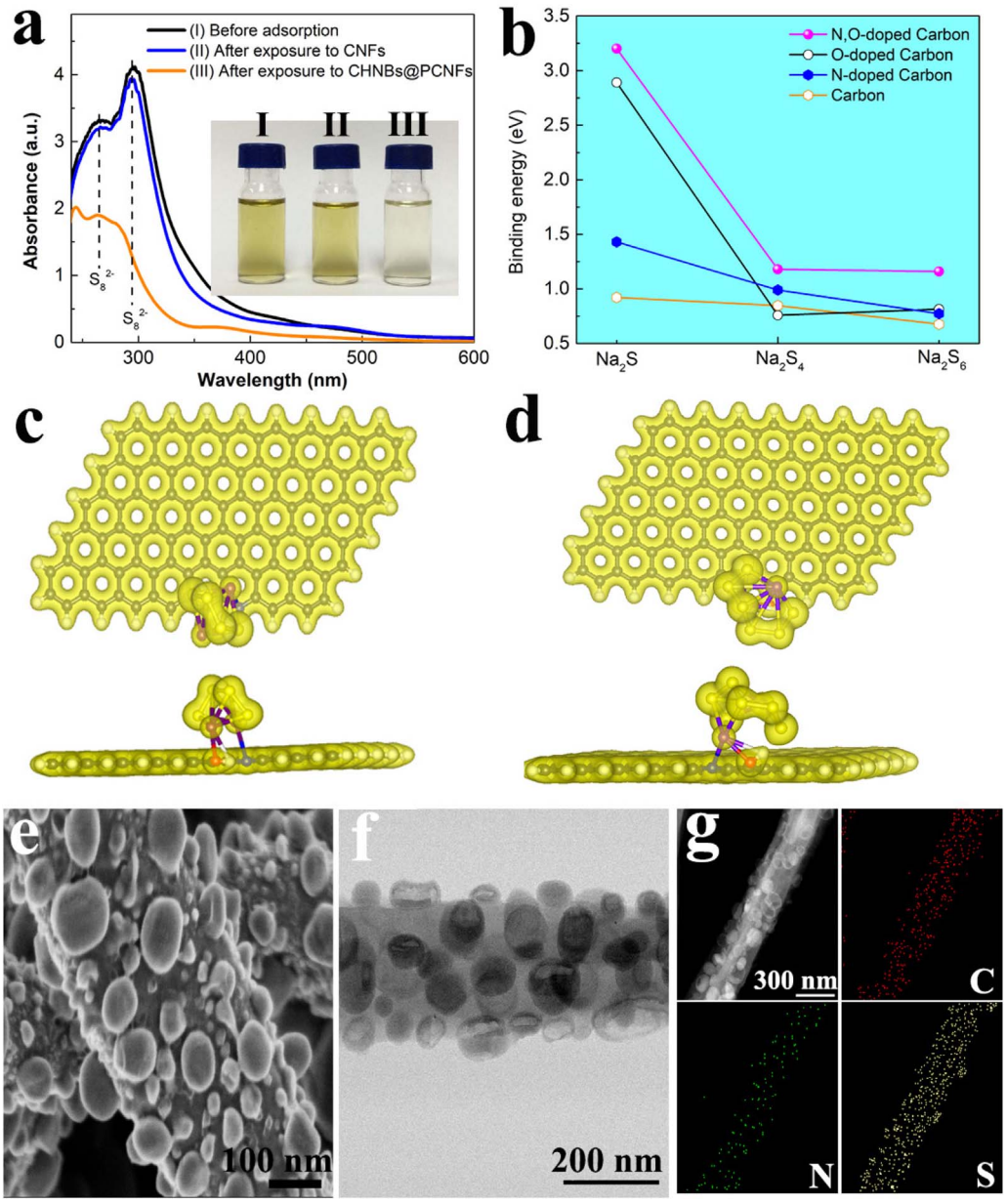

Fig. 3. (a) UV-vis spectra and corresponding photograph (inset) of the pure NaPSs solution (I) and the solution after exposure to the different substances: (II) CNFs, and (III) CHNBs@PCNFs (photographs taken after the solutions were allowed to stand for 30 min). (b) Comparison of the binding energy of various NaPSs molecules binding to the pure carbon, O-doped carbon, N-doped carbon, and N, O-codoped carbon, respectively. Atom positions and charge density plot of Na_2S_4 (c) and Na_2S_6 (d) molecular interaction with N, O-codoped carbon. Grey, white, blue, yellow, purple, and red balls represent C, H, N, S, Na, and O atoms, respectively. (e) SEM and (f) TEM images of S/(CHNBs@PCNFs). (g) Scanning (STEM) image and the corresponding elemental mapping of S/(CHNBs@PCNFs).

accordingly changes from yellow to ruby red, which is the characteristic color of the Li_3N resulting from the decomposition of metal azides, and the SEM images verify the formation of massive nanobubbles on the surfaces of the 1D fibrous structures at this stage (Fig. S8). XRD patterns (Fig. S3) also confirm the formation of Li_3N upon thermal heating to 240 °C. These results directly demonstrate that the generation of nanobubbles is derived from the repulsive force of the N_2 that is liberated by the decomposition of LiN_3. Finally, after carbonization at 650 °C for 180 min, the color of the films becomes black, and the 1D architecture is well maintained, in which CHNBs are uniformly formed on the surfaces of PCNFs, leading to the formation of CHNBs@PCNFs.

To further unravel the role of LiN_3 in tuning the nanostructure of the as-synthesized PCNFs, a series of control experiments were carried out. It could be clearly observed that, as expected, the size and density of CHNBs increased, in general, with an increase in the weight ratio of LiN_3 to PVA in the electrospinning precursors (Table S1). More interestingly, based on the fact that the generation of CHNBs and hierarchical pores inside the CNFs results from the decomposition of LiN_3, it is proposed that the morphology of CHNBs could be easily controlled by tuning the decomposition rate of LiN_3, which was facilely adjusted by changing the heating rate during the process of carbonization. SEM images (Table S2) demonstrate that, when the weight ratio of LiN_3 to PVA is fixed at 21.5%, the increased diameter and density of the as-formed CHNBs are closely correlated with decreased heating rates within a certain range from 1 to 0.5 °C min^{-1}. Many open pores were generated on the surfaces of the CNFs instead of the formation of CHNBs due to the explosive release of nitrogen when the heating rate is 2 °C min^{-1}. This result obviously confirms that the heating rate plays a critically important role in tuning the formation of CHNBs on the surfaces of PCNFs, *i.e.*, the explosive release of N_2 with a relatively higher heating rate will push away the PVA surrounding LiN_3 and then burst out, leading to the formation of pores on the surface, while the

gentle desorption of N_2 at a lower heating rate could slowly blow up the surrounding PVA, leading to the formation of CHNBs on the surface after carbonization. Therefore, the nanoarchitecture of the as-synthesized CHNBs@PCNFs could be facilely controlled by simply changing the concentration of LiN_3 and the heating rate for carbonization, which provides great potential for their applications in various fields.

To expand the application of LiN_3 as the pore generator, polyvinyl pyrrolidone (PVP) was further adopted as the carbon precursor with the consideration of the solubility of PVP in water with LiN_3 and the wide application of PVP in electrospinning. Although the calcination of PVP-LiN_3 nanofibers through the same procedure leads to the fabrication of CNFs with the fibrous structure, no pores as observed in the CHNBs@PCNFs are present (Fig. S9). TGA results exhibit that, in contrast with PVA-LiN_3 NFs, there is no violent decomposition step of LiN_3 during the carbonization of PVP-LiN_3 NFs (Fig. S6). Moreover, it could be clearly observed that the weight loss of PVP-LiN_3 NFs is much lower than that of pure PVP NFs. These results demonstrate the reaction between LiN_3 and PVP upon thermal heating, which leads to the loss of LiN_3 as the pore generator.

The carbon structure of CHNBs@PCNFs was subsequently investigated by Raman spectroscopy, in which two broad peaks located at 1326 and 1584 cm^{-1} could be assigned to typical D- and G-bands of carbon, respectively (Fig. S10). The intensity ratio of the D to the G-band of CHNBs@PCNFs was calculated to be 1.08, indicating the presence of abundant defects and vacancies, which could not only promote the diffusion of sodium ions, but also provide more intercalation sites for sodium storage [32]. The chemical composition and chemical bonding states of CHNBs@PCNFs were investigated by X-ray photoelectron spectroscopy (XPS) and elemental analysis. XPS spectra of the CHNBs@PCNFs composite exhibit the presence of C, N, and O (Fig. S11), with no other impurities detected. N doping with a dopant content of 5.2% is derived from the reaction between the Li_3N generated by the decomposition of LiN_3 and PVA during the carbonization process [33]. It could be supported by XRD results, which confirms the disappearance of Li_3N and the formation of Li_2CO_3 before washing and drying (Fig. S3). The C 1 s XPS profile of CHNBs@PCNFs demonstrates the presence of C-C/C=C bonds and oxygen-containing functional groups, as well as the formation of C-N bonds (Fig. S12a), while the high-resolution N 1 s spectrum of CHNBs@PCNFs could be resolved into three different peaks, which correspond to pyridinic N at 399.2 eV, pyrrolic N at 400.5 eV, and graphitic N at 401.9 eV, respectively (Fig. S12b). The doping of these electron-rich heteroatoms, *i.e.*, O and N, could produce abundant active sites and tune the surface electronic structure of the carbon materials, thus promoting the surface affinity for polysulfides [34–36]. The ability of CHNBs@PCNFs to absorb NaPSs was first evaluated by ultraviolet-visible (UV-vis) spectroscopy before and after exposure to CNFs and CHNBs@PCNFs (Fig. 3a). The solution exposed to CHNBs@PCNFs exhibited much lower peak intensities of characteristic bands of NaPSs than those containing CNFs or the fresh solution without additives, indicating the strong adsorption capability of CHNBs@PCNFs derived from nitrogen- and oxygen-doping. Further evidence is provided by the lighter color of the NaPSs solution after exposure to CHNBs@PCNFs (inset of Fig. 3a), which becomes almost colorless within 30 min. By comparison, the solution exposed to CNFs remains intensely yellow, suggesting extremely weak interaction between the nonpolar CNFs and the polar NaPSs.

In order to examine the remarkable adsorption of heteroatom-doped CHNBs@PCNFs on NaPSs, first principles calculations were conducted based on density functional theory (DFT) to obtain the binding geometries and energies. As shown in Fig. 3b, the binding energies of Na_2S, Na_2S_4, and Na_2S_6 systems over the N, O-codoped carbon were calculated to be 3.2, 1.18, and 1.16 eV, respectively, which are much higher than the corresponding values on N-doped, O-doped, and non-doped carbon (Fig. S13). This indicates that nitrogen and oxygen codoping into carbon surfaces is more effective for adsorbing and trapping various polysulfides than the other carbon-based surfaces, which could effectively alleviate the shuttle effect of Na-S batteries. The optimized geometry indicates that the Na-O distance in Na_2S_4-N, O-codoped carbon is 2.428 Å, quite close to that in the crystalline phase of Na_2O (2.403 Å), which suggests the formation of the Na-O ionic bond, while the Na-N distance is 3.018 Å, only 0.649 Å longer than that in the crystalline phase of Na_3N (Fig. S14). More interestingly, the Na-N and Na-O distances in the adsorption geometry of Na_2S_6 on N, O-codoped carbon are 2.387 and 2.414 Å, respectively, and both are comparable to the corresponding bond lengths in the crystalline phases of Na_3N and Na_2O, validating the formation of Na-N and Na-O ionic bonds in this system. The charge density distribution maps (Fig. 3c, d) demonstrate that terminal Na atoms in NaPSs tend to directly bind to N and O atoms that have been dual-doped into carbon with a distinctive electron concentration between them, which suggests that the lone pair electrons of N and O atoms could interact with Na toms. This leads to a strong Na-N/O ionic bond interaction between the soluble NaPSs and the N, O-codoped carbon, which could effectively preserve the active materials and restrict the shuttle effect.

Considering its structural stability, with sufficient pore volume for accommodating a high loading ratio of sulfur to improve the energy density of Na-S batteries, CHNBs@PCNFs synthesized according to the optimized LiN_3/PVA ratio of 21.5% under a heating rate of 0.5 °C min^{-1} were selected for further investigation. Sulfur was infiltrated into the CHNBs@PCNFs via a facile melt-infiltration method, and it could be clearly observed that the as-prepared composite maintains a long, continuous fibrous structure (Fig. 3e). In addition, the diameter and shell thickness of CHNBs were well preserved, and no aggregated sulfur particles were exposed on the surface, indicating the complete diffusion of sulfur into the void spaces of CHNBs@PCNFs. The darker region inside every CHNB after sulfur infiltration compared to the pure CHNBs indicates the successful loading of sulfur (Fig. 3f). Energy dispersive spectroscopy (EDS) elemental mapping obviously verifies the uniform distribution of C, N, and S in the CHNBs@PCNFs (Fig. 3g), and the signal of sulfur is also uniformly well matched with the CHNBs on PCNFs. These results demonstrate the homogeneous confinement of sulfur within the entire CHNBs@PCNFs sample. Further evidence is provided by the drastic decrease in surface area and pore volume after sulfur infiltration according to the nitrogen absorption-desorption isotherms (Fig. S4). It is interesting to notice the partial preservation of the pores and large empty volume after the infiltration process, which agrees well with the TEM results, and could effectively accommodate the volume changes of S in the electrochemical reactions during cycling. The X-ray diffraction (XRD) pattern of S/(CHNBs@PCNFs) composite reveals the presence of weak signals belonging to sulfur with the same orthorhombic structure as elemental sulfur powder (Fig. S15). The sulfur content was determined to be approximately 71.2% by thermogravimetric analysis (TGA) (Fig. S16). It should be noted that S/(CHNBs@PCNFs) exhibits a higher sulfur vaporization temperature than pure sulfur or S/CNFs, which suggests the strong absorption of sulfur by the CHNBs@PCNFs and the incorporation of sulfur into the small pores of the carbon framework. Additionally, the signal of sulfur is undetectable in Raman spectra of S/(CHNBs@PCNFs) (Fig. S10), suggesting a good distribution of S inside CHNBs@PCNFs without any obvious aggregation, corresponding well with the SEM and TEM results.

The electrochemical properties of S/(CHNBs@PCNFs) cathodes were evaluated by assembling them into Na-S batteries with Na-foil as an anode. Cyclic voltammetry (CV) of the resultant Na-S battery was conducted in the voltage range from 1.2–2.8 V at a scan rate of 0.1 mV s^{-1}. In the first cycle, the cathodic peaks at 2.22 and 1.42 V are attributed to the reduction of sulfur to long-chain NaPSs (e.g., Na_2S_n, $4 \le n \le 8$) and short-chain sodium sulfides (e.g., Na_2S_2) or sodium sulfide (Na_2S) [17,37]. XRD patterns (Fig. S17) demonstrate the formation of NaPSs and Na_2S in the discharged products of S/(CHNBs@PCNFs) cathodes after being discharged to 2.0 V and 1.2 V, respectively. In

addition, as shown in the HRTEM images (Fig. S18), after being discharged to 2.0 V, the d-spacings of the crystalline nanoparticles in the S/(CHNBs@PCNFs) cathodes were measured to be 0.44 and 0.48 nm, corresponding to the (100) planes of Na_2S_5 and the (200) planes of Na_2S_4, while the d-spacings of the S/(CHNBs@PCNFs) cathodes being dicharged to 1.2 V could be acribed to the (111) planes of Na_2S, in good agreement with the XRD results. High-resolution S 2p spectra provides further evidence to the formation of Na_2S as well as the absence of sulfur after the initial full discharge process (Fig. S19). In the anodic process, two peaks at around 1.87 and 2.41 V, corresponding to the conversion of sodium sulfides to polysulfides and sulfur, respectively, are observed [17,37]. After the initial full charge process, although no visible peak is observed in the XRD patterns of S/(CHNBs@PCNFs) cathodes, which indicates the amorphous state of the charged products without long-range order, the characteristic peaks belonging to sulfur could be clearly observed in the XPS spectra with the disappearance of NaPSs and Na_2S, which suggests the transformation of NaPSs and Na_2S back to sulfur. Those results confirm the conversion reaction of sulfur upon cyling charge-discharge process, accounting for the reversible electrochemical capacity. After the electrochemical activation during the first cycle, two pairs of obvious redox peaks at 2.23/2.41 and 1.52/1.87 V, corresponding to reversible transitions between elemental sulfur, long-chain NaPSs, and short chain sodium sulfide, respectively, are present in the subsequent sweeps. The CV profiles remained unchanged after the first two cycles without any noticeable peak shift, indicating the excellent stability and high reversibility of S/(CHNBs@PCNFs). The galvanostatic charge/discharge behavior of the S/(CHNBs@PCNFs) cathode was subsequently investigated at a rate of 0.1 C (1 C = 1675 mA g^{-1}). Two plateaus were observed at ~ 1.48 and 2.22 V in the discharge process, which were attributed to the two-stage reduction of elemental sulfur to long-chain NaPSs and then to Na_2S_2/Na_2S, respectively, which agrees well with the CV results. The S/(CHNBs@PCNFs) cathode delivers an initial specific discharge capacity of 1214 mA h g^{-1} at the rate of 0.1 C, corresponding to 72.6% sulfur utilization, based on the theoretical value of sulfur (1672 mA h g^{-1}), and gains a reversible specific capacity of 913 mA h g^{-1} in the first charge. It should be noted that the contribution of CHNBs@PCNFs could be ignored due to its low specific capacity of 48 mA h g^{-1} in the given potential range and its low weight ratio in the composite (Fig. S20). These initial specific capacities are much higher than those of the S/CNFs (394 mA h g^{-1}) and sulfur (48 mA h g^{-1}) electrodes (Fig. 4c). The coulombic efficiency of the electrode quickly stabilizes to > 95% within 10 cycles. After 50 cycles, the S/(CHNBs@PCNFs) cathode still maintains a high reversible capacity of 786 mA h g^{-1}, corresponding to a capacity retention of 65%, which indicates its good cycling stability, which is due to the strong adsorption capability of CHNBs@PCNFs towards NaPSs. By comparison, the S/CNFs electrode exhibits much lower sulfur utilization and poor cycling performance.

To understand the role of CHNBs@PCNFs in improving the performance of Na-S batteries, the batteries were disassembled after 50 cycles of discharge and charge process and postmortem SEM analysis was conducted on the pure sulfur, S/CNFs and S/(CHNBs@PCNFs) electrodes (Fig. S21). It is revealed that, due to the redeposition of insoluble Na_2S/Na_2S_2 species on the cathode surface, a thick layer of glassy discharge products is formed on the pure sulfur electrode with the serious aggregation of sulfur after cycling discharge and charge process derived from the redisposition of insoluble Na_2S/Na_2S_2 species, which is similar with the phenomenon observed in Li-S batteries [38–40]. Although this phenomenon is alleviated to a certain extent when using CNFs as the host of sulfur, the aggregation of sulfur is still apparently present, which suggests the dissolution loss of active sulfur into the electrolyte due to the lack of spatial confinement and weak binding between CNFs and NaPSs during electrochemical reactions, leading to the inhomogeneous deposition of Na_2S/Na_2S_2 species. By comparison, no glassy discharge products on the surface of the S/(CHNBs@PCNFs) electrode after 50 cycles were observed and strong sulfur signals are uniformly distributed within the whole electrode, which indicates the effective absorption and trapping of polysulfides within CHNBs@PCNFs. Thus, the utilization of the active sulfur materials was significantly enhanced via adopting CHNBs@PCNFs as the host of sulfur. These results validate that CHNBs@PCNFs could effectively restrict the diffusion of soluble sodium polysulfides, which would improve the utilization of sulfur and the cycling stability.

Rate tests of S/(CHNBs@PCNFs) cathode at different current rates exhibited an excellent high-rate capability. On increasing the current rate to 0.2, 0.5, and 1C, the S/(CHNBs@PCNFs) cathode could deliver high discharge capacity of 709, 598, and 487 mA h g^{-1}, respectively. Even at a high current density of 2 C, a high reversible capacity of 304 mA h g^{-1} could still be achieved. After completing the 2C rate measurement, a high reversible capacity of 790 mA h g^{-1} was retained, indicating fast electrochemical reactions kinetics of the electrode and the good electrode integrity. In comparison, the average specific capacity of S/CNFs cathode fades drastically from 415 to 74 mA h g^{-1} as the rate increases from 0.1 to 2C. The long-term cycling stability of the S/(CHNBs@PCNFs) cathode was also investigated at the high rate of 2C, and it presented a high specific capacity as well as good cycling retention. After 400 cycles, the S/(CHNBs@PCNFs) cathode still retained a high capacity of 256 mA h g^{-1} (specific energy density: 384 W h kg^{-1}) with a low decay rate of 0.044% per cycle. More importantly, the average Coulombic efficiency of the Na-S battery containing the S/(CHNBs@PCNFs) cathode was approaching 100% throughout the whole long-term cycling test, exhibiting great potential for the practical application of high-energy and long-life Na-S batteries. To the best of our knowledge, the rate and cycling performance of S/(CHNBs@PCNFs) is the best performance among carbon-based sulfur electrodes (Table S3). The excellent reversibility, high capacity, and superior cycling performance of S/(CHNBs@PCNFs) could be attributed to the unique features of CHNBs@PCNFs as sulfur host: (1) CHNBs on 1D PCNFs, with high aspect ratio and abundant pores, can effectively facilitate the transportation of electrolyte and buffer the mechanical stresses generated by the volume variation of S cathode during cycling; (2) CHNBs could not only provide abundant room to accommodate sulfur, but also act as a polysulfide reservoir through chemical adsorption to alleviate the shuttle effect, leading to significantly improved cycling stability; (3) The integrated 1D structure of PCNFs provides continuous conductive pathways, which could aid in rapid electron transfer within the insulating sulfur confined in the isolated bubbles, i.e., CHNBs, resulting in high sulfur utilization and hence reversible capacity.

The unique architecture of CHNBs@PCNFs, *i.e.*, large pore volume, hierarchical pores, and robust structure, could be considered as containing promising nanoscale building blocks for functional materials. To elucidate, in this work, CHNBs@PCNFs were further investigated as a stable structural framework to support MgH_2 nanocrystals (NCs) as hydrogen storage materials. Due to its high gravimetric (7.6 wt.% H_2) and volumetric (109 g H_2 L^{-1}) hydrogen capacities, high abundance, low cost, and high safety, MgH_2 represents a highly promising candidate for hydrogen storage [3]. The practical application of MgH_2, however, is strongly obstructed by its thermodynamic stability and slow kinetics for reversible hydrogen storage [41]. One of the most effective strategies to relieve the kinetic barrier and/or thermodynamic stability is to disperse MgH_2 nanocrystals (NCs) into porous hosts, which could directly decrease the solid-state diffusion distance for hydrogen storage and increase the surface-to-volume ratio of particles, leading to a significantly enhanced hydrogen storage performance [42–44]. Nonetheless, owing to the lack of control over the infiltration process and the highly limited porosity of the adopted hosts, inhomogeneous particle sizes, irregular spatial distributions, and low infiltration efficiency hinder the application of this strategy for improving the hydrogen storage properties of MgH_2 [45]. The unique structure and nature of CHNBs@PCNFs, however, is capable of dispersing MgH_2

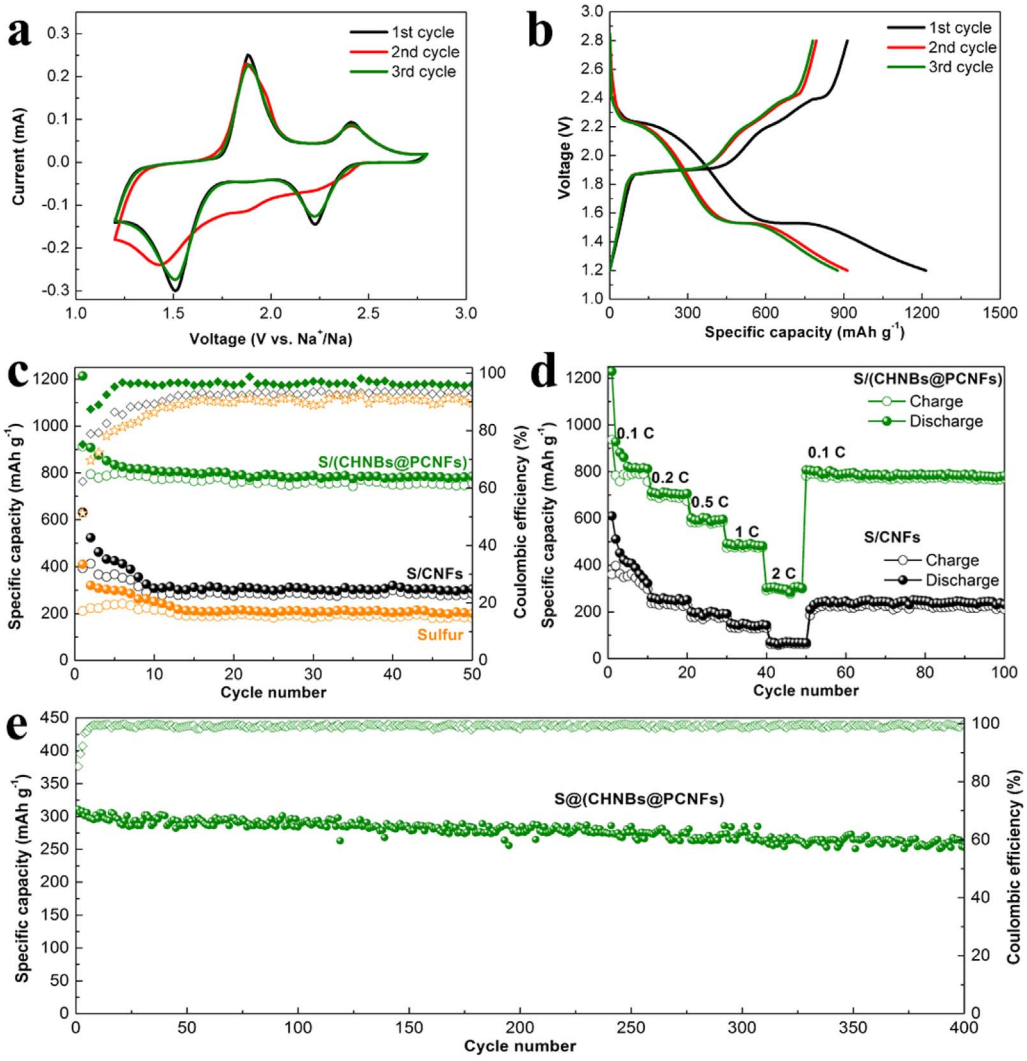

Fig. 4. Electrochemical performance of the S/(CHNBs@PCNFs) electrode in Na-S batteries. (a) Cyclic voltammograms for the initial three cycles of the S/(CHNBs@PCNFs) electrode at a scanning rate of 0.2 mV s^{-1}. (b) Galvanostatic discharge-charge profiles for the first 3 cyles at a current density of 0.1 C. (c) Cycling performance at a current density of 0.1 C and coulombic efficiency of S/(CHNBs@PCNFs) electrode, with S@CNFs included for comparison. (d) Rate performance at different current densities from 0.1 C to 2 C, with S@CNFs and pure sulfur included for comparison. (e) Cycling performance at a current density of 2 C.

NCs and further improving their hydrogen storage performance. First, the hierarchical porous structure of CHNBs@PCNFs with large pore volume provides sufficient void space for anchoring MgH_2 NCs. More importantly, the favorable interaction between the precursor of MgH_2, *i.e.*, di-n-butylmagnesium, and the carbon framework could ensure the homogeneous distribution of the thus-formed MgH_2 NCs from di-n-butylmagnesium on CHNBs@PCNFs and promote further reduction of particle size [46]. Furthermore, the catalytic effect of carbon in CHNBs@PCNFs could play an important role in further enhancing the hydriding and dehydriding performance of MgH_2[47,48] and the presence of abundant open channels in CHNBs@PCNFs would facilitate fast transportation of hydrogen and the adopted precursors.

As shown in Fig. 5a, MgH_2 NCs supported on CHNBs@PCNFs were realized by the self-assembly strategy using solvothermal treatment of di-n-butylmagnesium solution in cyclohexane under 3.5 MPa hydrogen pressure [46]. After solvothermal treatment in cyclohexane at 200 °C for 24 h, CHNBs@PCNFs retain their primary morphology owing to its robust structure, and the surface of CHNBs is no longer smooth but has become an anchoring site for a multitude of nanoparticles (Fig. 5b). From the high-magnified TEM image (Fig. 5c), the average particle size of MgH_2 NCs is measured to be approximately 5.1 nm (Fig. S22), which could significantly improve the hydrogen storage properties of MgH_2, owing to shortened diffusion distances and increased surface energy[49–51], while a certain amount of space between these MgH_2 NCs that are homogenously anchored on the CHNBs of CHNBs@PCNFs (MgH_2/(CHNBs@PCNFs)) could effectively alleviate the agglomeration and growth of the MgH_2 NCs during thermal heating for hydrogen storage. The high-resolution TEM (HRTEM) image (inset of Fig. 5c) confirms that the lattice fringes of the nanoparticles have a spacing of ~ 0.250 nm, which corresponds well with the (101) planes of MgH_2 and is consistent with the XRD (Fig. S23) patterns. The elemental mapping in Fig. 5d confirms that the C and Mg maps correspond well with the structure of CHNBs@PCNFs, demonstrating the homogeneous distribution of MgH_2 NCs both on the CHNBs and inside the PCNFs.

The dehydriding process for MgH_2/CHNBs@PCNFs was first characterized by TGA and mass spectroscopy (MS). It should be noted that all the hydrogen capacity is calculated on the basis of MgH_2 in the composite (Fig. 6a). The ball-milled MgH_2 and CHNBs@PCNFs exhibits a dehydrogenation peak at 323 °C (Fig. 6b), 48 °C lower than for bulk MgH_2, which demonstrates the catalytic role of CHNBs@PCNFs on the hydrogen storage process of MgH_2. In strong contrast, H_2 evolution of MgH_2/(CHNBs@PCNFs) occurs in the temperature range of 205–320 °C

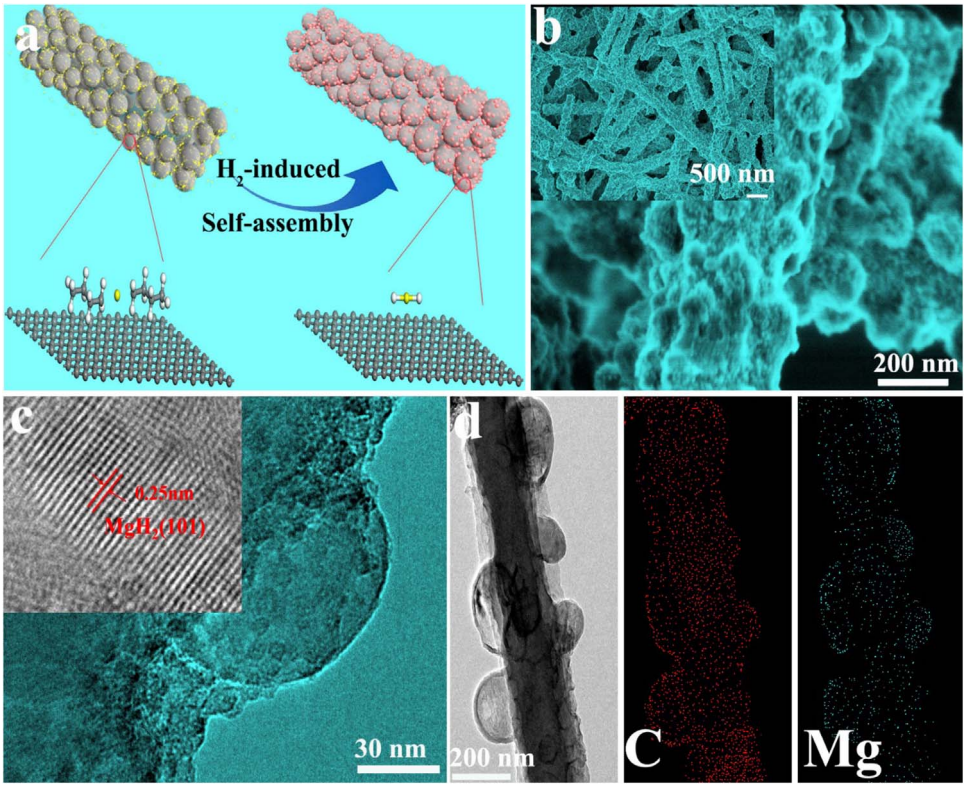

Fig. 5. (a) Schematic illustration of the preparation of MgH_2/(CHNBs@PCNFs) through the hydrogenation-induced self-assembly strategy. Grey, white, and yellow spheres are C, H, and Mg atoms, respectively. (b) SEM and (c) TEM images of MgH_2/(CHNBs@PCNFs) under different magnifications (with the inset of c showing an HRTEM image). (d) TEM image and the corresponding elemental mapping of MgH_2/(CHNBs@PCNFs).

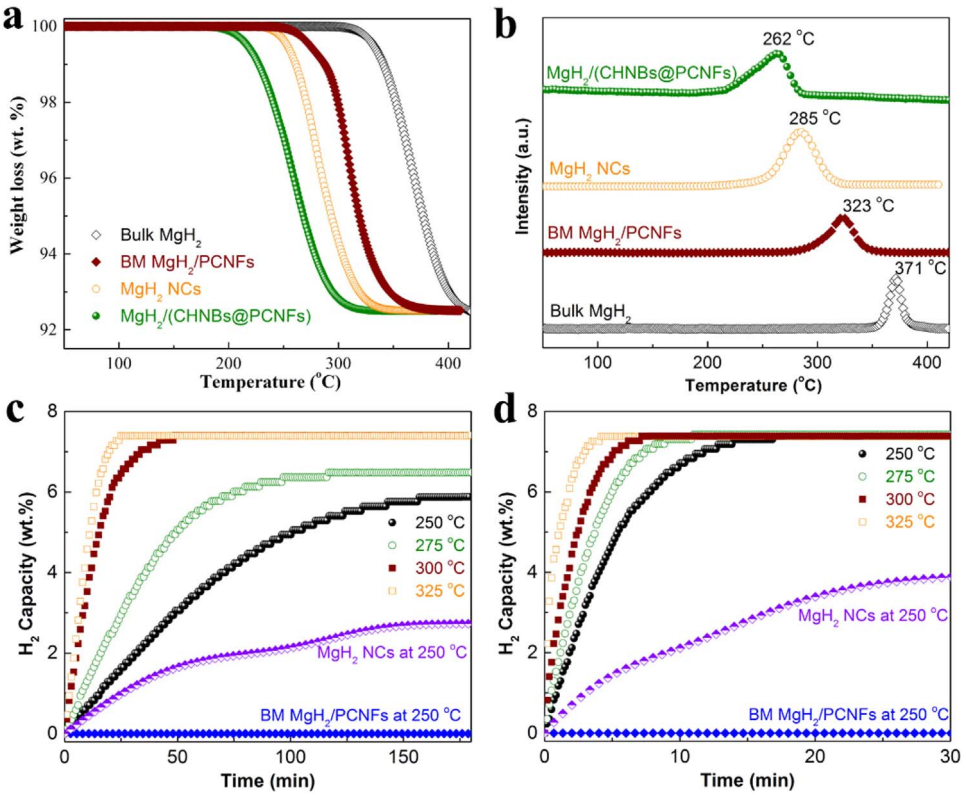

Fig. 6. TGA (a) and MS (b) profiles of MgH_2/(CHNBs@PCNFs), with bulk MgH_2, a ball-milled (BM) composite of MgH_2 and CHNBs@PCNFs (BM MgH_2/PCNFs), and MgH_2 NCs included for comparison. Isothermal dehydrogenation (c) and hydrogenation (d) profiles of MgH_2/(CHNBs@PCNFs) at different temperatures.

with a peak temperature of 265 °C (Fig. 6b), 23 °C and 61 °C lower than for MgH_2 NCs without CHNBs@PCNFs and the ball-milled composite, respectively. This verifies the significant synergistic role of both the catalytic effects of CHNBs@PCNFs and the reduction of particle size down to the nanometer range towards improving the dehydrogenation process of MgH_2. The dehydriding and hydriding kinetics of MgH_2/(CHNBs@PCNFs) was further investigated by isothermal dehydrogenation and hydrogenation at various temperatures (Fig. 6c and d). When heated at 250 °C, only ~ 2.8 wt.% H_2 could be released from MgH_2 NCs within 200 min, and no hydrogen release was observed for the ball-milled composite, while MgH_2/(CHNBs@PCNFs) could desorb 5.9 wt.% hydrogen within the same period. Moreover, 7.5 wt.% hydrogen, approaching the theoretical value of MgH_2, could be released in less than 25 min when the temperature was increased to 325 °C (Fig. S23). In terms of the reversible hydrogenation, 7.4 wt.% H_2 could be absorbed by MgH_2/(CHNBs@PCNFs) within 15 min, even at a temperature as low as 250 °C, while only 3.9 wt.% H_2 was taken up for the MgH_2 NCs without the support of CHNBs@PCNFs, and the ball-milled composite exhibited no hydrogenation under the same conditions. More importantly, a complete hydrogenation process, with a capacity of 7.5 wt.%, was observed for MgH_2/(CHNBs@PCNFs) in less than 7 min at 325 °C. The apparent activation energies (E_a) for dehydrogenation and hydrogenation of MgH_2/(CHNBs@PCNFs) were subsequently calculated according to the Arrhenius equation to quantitatively evaluate the significantly improved dehydriding/hydriding kinetics. After fitting the experimental data at various temperature (Fig. S24), the activation energy for dehydrogenation and hydrogenation of MgH_2/(CHNBs@PCNFs) was calculated to be 76.4 and 67.1 kJ mol^{-1}, respectively, which is significantly lower than the values reported for their bulk counterpart (*i.e.*, 158.5 kJ mol^{-1} for dehydrogenation and 99.0 kJ mol^{-1} for hydrogenation) [52] and for pure MgH_2 NCs (*i.e.*, 126 kJ mol^{-1} for dehydrogenation) [53] synthesized under the same conditions without the presence of CHNBs@PCNFs. These results obviously confirm the significant improvement of the hydrogenation and dehydrogenation kinetics of MgH_2 owing to the catalytic role of CHNBs@PCNFs, the much shortened diffusion pathways resulting from the tremendous reduction in particle size to only 5.1 nm, and the homogenous dispersion of MgH_2 NCs on CHNBs@PCNFs, which could further facilitate the catalytic effects of CHNBs@PCNFs.

3. Conclusions

In summary, we have demonstrated a novel and general strategy, namely, a scalable and low-cost bubbling-assisted electrospinning method, for producing hierarchical porous carbon nanofibers with a sophisticated structure. By facilely altering the decomposition rate and the amount of bubbling agent, controllable fabrication of carbon hollow nanobubbles on porous carbon nanofibers could be achieved. Benefiting from the excellent electrical conductivity and strong chemical adsorption capability towards NaPSs, CHNBs@PCNFs has been demonstrated to be an ideal sulfur host for room-temperature Na-S batteries, while the as-synthesized S/(CHNBs@PCNFs) cathode delivered a high reversible capacity of 913 mA h g^{-1} at 0.1 C, and exhibited a stable cycle life up to 400 cycles with a small capacity decay of 0.044% per cycle and a Coulombic efficiency approaching 100%. When CHNBs@PCNFs are used as a structural support for MgH_2 NCs, a complete dehydrogenation at a temperature as low as 250 °C is realized within only 15 min due to the catalytic role of CHNBs@PCNFs and the homogenous dispersion on them of MgH_2 NCs with a particle size of 5.1 nm. This unique synthetic concept represents a new avenue for the preparation of multifunctional hierarchical porous carbon materials and has great potential for scalable and low-cost industrial production of 1D nanostructured carbon materials.

4. Experimental details

4.1. Preparation of CHNBs@PCNFs

The raw materials PVA (Mv ≈ 88000, Alfa Aesar) and LiN_3 (20 wt. %, Alfa Aesar) were commercially available and directly used without further purification. Typically, PVA (0.5 g) was dissolved in deionized water (5 mL) at 90 °C for 8 h. After cooling down to room temperature, LiN_3 solution (0.5 mL) was then added and vigorously stirred for 6 h make a homogeneous spinning dope. The resultant solution was transferred into a syringe with an 18-gauge blunt-tip needle for electrospinning. The flow rate of solution was approximately 500 μL h^{-1}, as controlled by a syringe pump (Longer, TJP-3A, China), and a grounded stainless steel plate was horizontally placed 10 cm from the needle to collect the nanowires. A high voltage of 15 kV was applied by a high-voltage power supply. The as-collected electrospun fibers were first dewatered at a temperature of 75 °C under dynamic vacuum for 15 h and then calcined to 650 °C for 3 h under dynamic N_2 atmosphere to obtain the CHNBs@PCNFs after washing with hydrochloric acid and drying.

4.2. Preparation of S(CHNBs@PCNFs)

A mixture of CHNBs@PCNFs and sulfur powder with a weight ratio of 1:4 was sealed in a glass bottle under argon protection, which was then heated at 155 °C for 12 h, Subsequently, the product was heated at 200 °C for 30 min under dynamic argon atmosphere to remove the redundant sulfur outside the CHNBs@PCNFs. The S/CNFs composite was prepared by the same method.

4.3. Preparation of MgH_2/(CHNBs@PCNFs)

MgH_2/(CHNBs@PCNFs) (MgH_2:C = 40:60) were synthesized by a wet-chemical method. 1.6 ml di-n-butylmagnesium solution in heptane was added to 40 ml cyclohexane in a pressure reactor vessel. The solution was then stirred and heated to 200 °C under 3.5 MPa hydrogen pressure. After 24 h, the MgH_2/(CHNBs@PCNFs) was obtained from the decomposition of di-n-butylmagnesium in cyclohexane. The precipitates were washed several times with cyclohexane. The obtained materials were further dried at room temperature under dynamic vacuum on a Schlenk line.

4.4. Adsorption test

Sodium polysulfide (Na_2S_8) was prepared by mixing 7 mol of S with 1 mol of Na_2S in tetraethylene glycol dimethyl ether (TEGDME) solvent. After mechanical stirring at 40 °C for 24 h in an Ar-filled glove box, a brownish-red Na_2S_8 solution was synthesized, which was then diluted to 1.25 mM for the polysulfide adsorption test. The adsorption test was conducted by immersing 15 mg of the as-synthesized CNFs and CHNBs@PCNFs in 2 mL of 0.005 M Na_2S_8 solution for 30 min. Digital photographs were taken after the solution was left to stand for 30 min.

4.5. Characterizations

The crystalline structure of the samples was characterized by X-ray diffraction (XRD) conducted on a Rigaku D/max-kA diffractometer with Cu Kα radiation. (An amorphous tape was used to prevent the oxidation and moisture contamination of samples during XRD measurements.) Nitrogen absorption/desorption isotherms (Brunauer–Emmett–Teller (BET) technique) at the temperature of liquid nitrogen were collected via a Quantachrome NOVA 4200e instrument to characterize the pore structure of the samples. Thermal property measurements were performed by thermogravimetry (TG, STA 409 C) with a heating rate of 5 °C min^{-1} under Ar. The microstructures were

observed by transmission electron microscopy (TEM, JEM-2100F, JEOL) and field-emission scanning electron microscopy (SEM, S-4800, Hitachi). The X-ray photoelectron spectroscopy (XPS) was conducted on a Perkin Elmer PHI 5000 C ESCA system equipped with a dual X-ray source, in which an Mg Kα (1253.6 eV) anode and a hemispherical energy analyser were used. The background pressure during data acquisition was maintained at < 10^{-6} Pa, and measurements were conducted at a pass energy of 93.90 eV. All binding energies were calibrated using contaminant carbon (C 1s = 284.6 eV).

4.6. Electrochemical measurements

CR2032 coin cells were assembled with sodium metal as the counter and reference electrodes in an argon-filled glove box. The S/CHNBs@PCNFs and S/CNFs cathode slurries were made by mixing 80 wt% active materials with 10 wt% carbon black and 10 wt% carboxyl methylated cellulose (CMC) in water by mortar and pestle. The resultant slurry was then casted on the aluminium foil using a doctor blade prior to drying in a vacuum oven at 60 °C for 20 h. The areal mass loading of sulfur in this study is controlled to be around 1.4 mg cm^{-2}. Glass fiber purchased from Whatman was used as the separator. The electrolyte used was 1 M sodium perchlorate ($NaClO_4$) in ethylene carbonate/propylene carbonate (EC/PC, 1:1 v/v%) with the addition of 5 wt.% fluoroethylene carbonate (FEC). The assembled cells were galvanostatically charged and discharged over the voltage range of 1.2–2.8 V versus Na/Na^+ at various constant current densities on a Land CT-2001A battery tester. Electrochemical impedance spectroscopy and cyclic voltammetry were performed on a VMP-3 electrochemical workstation at a scan rate of 0.1 mV s^{-1}.

4.7. Hydrogen storage measurements

The hydrogen storage properties of the thus-synthesized MgH_2/(CHNBs@PCNFs) were investigated on a Sieverts apparatus, described as a gas reaction controller (GRC, Advanced Materials Corp., USA). The hydriding kinetics measurements were performed with an initial pressure of 30 atm, and the dehydriding properties were detected at various temperatures under a hydrogen pressure below 0.02 atm. For the purposes of comparison, CHNBs@PCNFs were excluded when determining the capacity of hydrogen from the relevant composites.

Acknowledgements

This work was partially supported by the National Key Research and Development Program of China (2017YFA0204600), National Science Fund for Distinguished Young Scholars (51625102), the National Natural Science Foundation of China (51471053), and the Science and Technology Commission of Shanghai Municipality (17XD1400700). G. Xia is grateful for the financial support from ARC (DE170100362). The authors also would like to thank Dr. Tania Silver for critical reading of the manuscript.

Appendix A. Supporting information

Supplementary data associated with this article can be found in the online version at doi:10.1016/j.ensm.2018.05.008.

References

[1] Y. Sun, N. Liu, Y. Cui, Nat. Energy 1 (2016) 16071.
[2] B. Dunn, H. Kamath, J.-M. Tarascon, Science *334* (2011) 928.
[3] S.-i Orimo, Y. Nakamori, J.R. Eliseo, A. Züttel, C.M. Jensen, Chem. Rev. 107 (2007) 4111.
[4] P. Chen, M. Zhu, Mater. Today 11 (2008) 36.
[5] L. Schlapbach, A. Zuttel, Nature 414 (2001) 353.
[6] L. Schlapbach, Nature 460 (2009) 809.
[7] A. Manthiram, Y. Fu, S.-H. Chung, C. Zu, Y.-S. Su, Chem. Rev. 114 (2014) 11751.
[8] M. Wild, L. O'Neill, T. Zhang, R. Purkayastha, G. Minton, M. Marinescu, G.J. Offer, Energy Environ. Sci. 8 (2015) 3477.
[9] A. Manthiram, X. Yu, Small 11 (2015) 2108.
[10] S. Wei, S. Xu, A. Agrawral, S. Choudhury, Y. Lu, Z. Tu, L. Ma, L.A. Archer, Nat. Commun. 7 (2016) 11722.
[11] X. Lu, G. Xia, J.P. Lemmon, Z. Yang, J. Power Sources 195 (2010) 2431.
[12] Z. Wen, Y. Hu, X. Wu, J. Han, Z. Gu, Adv. Funct. Mater. 23 (2013) 1005.
[13] T.H. Hwang, D.S. Jung, J.-S. Kim, B.G. Kim, J.W. Choi, Nano Lett. 13 (2013) 4532.
[14] S. Wenzel, H. Metelmann, C. Raiß, A.K. Dürr, J. Janek, P. Adelhelm, J. Power Sources 243 (2013) 758.
[15] S. Xin, Y.-X. Yin, Y.-G. Guo, L.-J. Wan, Adv. Mater. 26 (2014) 1261.
[16] X. Yu, A. Manthiram, Adv. Energy Mater. 5 (2015) 1500350.
[17] X. Yu, A. Manthiram, ChemElectroChem 1 (2014) 1275.
[18] X. Yu, A. Manthiram, J. Phys. Chem. C 118 (2014) 22952.
[19] X. Yu, A. Manthiram, J. Phys. Chem. Lett. 5 (2014) 1943.
[20] Z. Qiang, Y.-M. Chen, Y. Xia, W. Liang, Y. Zhu, B.D. Vogt, Nano Energy 32 (2017) 59.
[21] R. Carter, L. Oakes, A. Douglas, N. Muralidharan, A.P. Cohn, C.L. Pint, Nano Lett. 17 (2017) 1863.
[22] L. Zeng, Y. Yao, J. Shi, Y. Jiang, W. Li, L. Gu, Y. Yu, Energy Storage Mater. 5 (2016) 50.
[23] Y.-X. Wang, J. Yang, W. Lai, S.-L. Chou, Q.-F. Gu, H.K. Liu, D. Zhao, S.X. Dou, J. Am. Chem. Soc. 138 (2016) 16576.
[24] I. Kim, C.H. Kim, S. h Choi, J.-P. Ahn, J.-H. Ahn, K.-W. Kim, E.J. Cairns, H.-J. Ahn, J. Power Sources 307 (2016) 31.
[25] Y.-X. Yin, S. Xin, Y.-G. Guo, L.-J. Wan, Angew. Chem. Int. Ed. 52 (2013) 13186.
[26] Z. Li, J.T. Zhang, Y.M. Chen, J. Li, X.W. Lou, Nat. Commun. 6 (2015) 8850.
[27] H.B. Wu, G. Zhang, L. Yu, X.W. Lou, Nanoscale Horiz. 1 (2016) 27.
[28] Z. Li, H.B. Wu, X.W. Lou, Energy Environ. Sci. 9 (2016) 3061.
[29] J.S. Lee, J. Jun, J. Jang, A. Manthiram, Small 13 (2017) 1602984.
[30] K. Mi, Y. Jiang, J. Feng, Y. Qian, S. Xiong, Adv. Funct. Mater. 26 (2016) 1571.
[31] G. Xia, D. Li, X. Chen, Y. Tan, Z. Tang, Z. Guo, H. Liu, Z. Liu, X. Yu, Adv. Mater. 25 (2013) 6238.
[32] Y. Liu, N. Zhang, L. Jiao, J. Chen, Adv. Mater. 27 (2015) 6702.
[33] G. Xia, L. Zhang, F. Fang, D. Sun, Z. Guo, H. Liu, X. Yu, Adv. Funct. Mater. 26 (2016) 6188.
[34] J. Song, Z. Yu, M.L. Gordin, D. Wang, Nano Lett. 16 (2016) 864.
[35] G. Zhou, E. Paek, G.S. Hwang, A. Manthiram, Adv. Energy Mater. 6 (2016) 1501355.
[36] J. Song, M.L. Gordin, T. Xu, S. Chen, Z. Yu, H. Sohn, J. Lu, Y. Ren, Y. Duan, D. Wang, Angew. Chem. Int. Ed. 54 (2015) 4325.
[37] X. Yu, A. Manthiram, Chem. Mater. 28 (2016) 896.
[38] G. Zhou, Y. Zhao, C. Zu, A. Manthiram, Nano Energy 12 (2015) 240.
[39] G. Zhou, Y. Zhao, A. Manthiram, Adv. Energy Mater. 5 (2015) 1402263.
[40] G. Zhou, E. Paek, G.S. Hwang, A. Manthiram, Nat. Commun. 6 (2015) 7760.
[41] K.-F. Aguey-Zinsou, J.-R. Ares-Fernandez, Energy Environ. Sci. 3 (2010) 526.
[42] H. Shao, G. Xin, J. Zheng, X. Li, E. Akiba, Nano Energy 1 (2012) 590.
[43] P.E. de Jongh, T.M. Eggenhuisen, Adv. Mater. 25 (2013) 6672.
[44] T.K. Nielsen, F. Besenbacher, T.R. Jensen, Nanoscale 3 (2011) 2086.
[45] M.L. Christian, K.-F. Aguey-Zinsou, ACS Nano 6 (2012) 7739.
[46] G. Xia, Y. Tan, X. Chen, D. Sun, Z. Guo, H. Liu, L. Ouyang, M. Zhu, X. Yu, Adv. Mater. 27 (2015) 5981.
[47] G. Liu, Y. Wang, L. Jiao, H. Yuan, ACS Appl. Mater. Interfaces 6 (2014) 11038.
[48] W. Cai, X. Zhou, L. Xia, K. Jiang, S. Peng, X. Long, J. Liang, J. Mater. Chem. A 2 (2014) 16369.
[49] Y. Jia, X. Yao, Int. J. Hydrog. Energy 42 (2017) 22933.
[50] Y. Liu, J. Zou, X. Zeng, W. Ding, RSC Adv. 4 (2014) 42764.
[51] Y.S. Au, M.K. Obbink, S. Srinivasan, P.C.M.M. Magusin, K.P. de Jong, P.E. de Jongh, Adv. Funct. Mater. 24 (2014) 3604.
[52] G. Liu, Y. Wang, C. Xu, F. Qiu, C. An, L. Li, L. Jiao, H. Yuan, Nanoscale 5 (2013) 1074.
[53] N.S. Norberg, T.S. Arthur, S.J. Fredrick, A.L. Prieto, J. Am. Chem. Soc. 133 (2011) 10679.